Using baseline-dependent window functions for data compression and field-of-interest shaping in radio interferometry

M.T. Atemkeng[1][*], O.M. Smirnov[12], C. Tasse[31], G. Foster[12], J. Jonas[12]

[1]*Department of Physics and Electronics, Rhodes University, PO Box 94, Grahamstown, 6140, South Africa*
[2]*SKA South Africa, 3rd Floor, The Park, Park Road, Pinelands, 7405, South Africa*
[3]*GEPI, Observatoire de Paris, CNRS, Universite Paris Diderot, 5 place Jules Janssen, 92190 Meudon, France*

ABSTRACT

In radio interferometry, observed visibilities are intrinsically sampled at some interval in time and frequency. Modern interferometers are capable of producing data at very high time and frequency resolution; practical limits on storage and computation costs require that some form of data compression be imposed. The traditional form of compression is a simple averaging of the visibilities over coarser time and frequency bins. This has an undesired side effect: the resulting averaged visibilities "decorrelate", and do so differently depending on the baseline length and averaging interval. This translates into a non-trivial signature in the image domain known as "smearing", which manifests itself as an attenuation in amplitude towards off-centre sources. With the increasing fields of view and/or longer baselines employed in modern and future instruments, the trade-off between data rate and smearing becomes increasingly unfavourable. In this work we investigate alternative approaches to low-loss data compression. We show that averaging of the visibility data can be treated as a form of convolution by a boxcar-like window function, and that by employing alternative baseline-dependent window functions a more optimal interferometer smearing response may be induced. In particular, we show improved amplitude response over a chosen field of interest, and better attenuation of sources outside the field of interest. The main cost of this technique is a reduction in nominal sensitivity; we investigate the smearing vs. sensitivity trade-off, and show that in certain regimes a favorable compromise can be achieved. We show the application of this technique to simulated data from the JVLA and EVN.

Key words: Instrumentation: interferometers, Methods: data analysis, Methods: numerical, Techniques: interferometric

1 INTRODUCTION

A radio interferometer measures complex quantities called *visibilities*, which, following the van Cittert-Zernike relation (Thompson 1999; Thompson et al. 2001), correspond to Fourier modes of the sky brightness distribution, corrupted by various instrumental and atmospheric effects. One particular effect, known as *time* and *bandwidth decorrelation* (or its equivalent in the image plane referred as smearing) occurs when the visibilities are averaged over a time and frequency bin of non-zero extent (Bridle & Schwab 1989, 1999). This unavoidably happens in the correlator (since the corre-

lator output is, by definition, an average measurement over some interval), and also if data is further averaged in post-correlation for the purposes of compression and to reduce computational cost.

The effect of smearing is mainly a decrease in the amplitude of off-axis sources. This is easy to understand: the visibility contribution of a point source of flux S located in the direction given by the unit vector $\boldsymbol{\sigma}$ is given by

$$V = S \exp \left\{ \frac{2\pi i}{\lambda} \boldsymbol{u} \cdot (\boldsymbol{\sigma} - \boldsymbol{\sigma}_0) \right\}, \qquad (1)$$

where $\boldsymbol{u}$ is the baseline vector (in a coordinate system fixed to the sky), and $\boldsymbol{\sigma}_0$ is the phase centre (or fringe stopping centre) of the observation. The complex phase term

[*] E-mail: m.atemkeng@gmail.com

above rotates as a function of frequency (due to the inverse scaling with λ) and time (due to the fact that $\boldsymbol{u}$ changes with time, at least in an Earth- or orbit-based interferometer). Taking a rotating complex vector average over a time/frequency bin then results in a net loss of amplitude. The effect increases with baseline length and distance from phase centre. Besides reducing apparent source flux, smearing also distorts the PSF, since different baselines (and thus different Fourier modes) are attenuated differently.

Throughout this work we use the term Field of Interest (FoI) which we differentiate from the Field of View (FoV). For this work the FoV is related to angular scale of the primary beam where as the FoI is a parameter of the scientific observation case, which may be related to the size of the primary beam but is not a necessary requirement. Thus, the FoI can be an adjustable parameter in the window functions we present.

In the era of large interferometers, where computation (and thus data size) becomes one of the main cost drivers, it is in principle desirable to average the data down as much as possible, without compromising the science goals. There are natural limits to this: firstly, we still need to critically sample the uv-plane, secondly, we need to retain sufficient spectral resolution, thirdly, we do not want to average (at least pre-calibration) beyond the natural variation of the calibration parameters, and fourthly, we want to keep smearing at acceptable levels in order not to lose too much signal. In this work, we concentrate specifically on the decorrelation/smearing problem. Typical observation cases are:

• Surveys where it is desirable to have a flat response across the largest possible FoI. This can be achieved by facet imaging but at a computatinal cost. By increasing the size of the facets a better balance between computional cost and image response can be acheived.

• Deep imaging where the it is useful to supress bright sources in the primary beam sidelobes outside of the FoI. Even with smearing of sources far from the phase centre bright sources can contribute significant flux and PSF sidelobe artefacts to the image..

• Very Long Baseline Interferometry (VLBI), decorrelation is more severe, so the effective FoI is determined by the smallest time/frequency bin size that a correlator can support, and is normally much smaller than the primary beam (Keimpema et al. 2015). Modern VLBI correlators overcome this by employing a technique where the signal is correlated relative to multiple phase centres simultaneously, thus effectively "tiling" the primary beam by multiple FoIs. This has a computational cost that scales linearly with the number of phase centres.

Smearing can be seen to be a useful side effect, anything outside the desired FoI (by definition) is unwanted signal. The primary beam pattern of any real antenna features sidelobes and backlobes that extend across the entire sky, albeit at a relatively faint level. The faintness makes sidelobes useless for imaging any but the brightest sources. However, the sum total signal from all the sources in the primary beam sidelobes, modulated by their PSF sidelobes, contributes an unwanted global background called the *far sidelobe confusion noise* (FSCN), in very deep observations this may in pricniple become a bottleneck (Smirnov et al. 2012). In other cases, individual extremely bright radio sources such

as Cygnus A or Cassiopeia A can contribute confusing signal from even the most distant sidelobe: the LOFAR telescope (Van Haarlem et al. 2013) has to deal with these so-called "A-team" sources on a routine basis. By suppressing distant off-axis sources, smearing somewhat alleviates both the FSCN and A-team problems.

When considering a short sequence of visibilities measured on one baseline, we can consider averaging as a convolution of the true visibility by a boxcar function corresponding to the uv-extent of the averaging bin, followed by sampling at the centre of each bin. Convolution in the visibility plane corresponds to multiplication of the image by an *image plane response function* that is the Fourier transform of the convolution kernel i.e the window function; the Fourier transform of a boxcar is a Sinc-type taper.

If we consider the entire uv-plane, averaging is only a pseudo-convolution, since the different uv-bins (and thus their boxcars) will have different sizes and shapes as determined by baseline length and orientation. Still, we can qualitatively view smearing as some kind of cumulative effect of an ensemble of image-plane tapers corresponding to all the different boxcars[1].

What if we were to employ weighted averaging instead of simple averaging (whether in the correlator, or in postprocessing)? This would correspond to a pseudo-convolution of the uv-plane by some ensemble of *window functions*, different from boxcars, which would obviously yield different image-plane tapers, and thus result in different smearing response. Filter theory suggests that a window function can be tuned to achieve some desired tapering response. An optimal taper would be one that was maximal across the desired FoI, and minimal outside it. In this work, we apply filter theory to derive a set of baseline-dependent window functions (BDWFs) that approximate this more optimal smearing behavior. The trade-off is an increase in thermal noise, since minimum noise can only be achieved with unweighted averaging. We show that this effect can be partially mitigated through the use of *overlapping window functions*. Offringa et al. (2012) have investigated a similar approach in the context of suppressing signals towards specific off-axis sources.

In the era of the Square Kilometre Array (SKA) and its pathfinders, where dealing with the huge data volumes is one of the main challenges, use of BDWFs potentially offers additional leverage in optimizing radio observations. Decreased smearing across the FoI allows for more aggressive data averaging, thus reducing storage and compute costs. The trade-off is a loss of sensitivity, which pushes up observational time requirements. However, the decrease in smearing and noise from A-team sources could, conceivably, make up for some of the nominal sensitivity loss. In the VLBI case, use of BDWFs potentially offers an increase in effective FoI at a given correlator dump rate, or equivalently, the ability to tile the

---

[1] For completeness, we should note that this "smearing taper" is not the only tapering effect at work in interferometric imaging. Firstly, antennas have a non-zero physical extent: a measured visibility is already convolved by the aperture illumination functions (AIFs) of each pair of antennas. The resulting image-plane taper is exactly what the primary beam is. Secondly, most imaging software employs convolutional gridding followed by an fast Fourier transform, which produces an additional taper that suppresses aliasing of sources from outside the imaged region.

primary beam with fewer phase centres, allowing for smaller correlators.

2 OVERVIEW AND PROBLEM STATEMENT

The following formalism deals with visibilities both as functions (i.e. entire distributions on the uv-plane), and single visibilities (i.e. values of those functions at a specific point). To avoid confusion between functions in functional notation and their values, we will use $\mathcal{V}$ or $\mathcal{V}(u,v)$ to denote functions, and V to denote individual visibilities. Likewise, $\mathcal{I}(l,m)$ denotes a function on the lm-plane i.e. an image. The symbol δ always denotes the Kronecker delta-function.

Depending on whether we want to consider polarization or not, $\mathcal{V}$ can be taken to represent either scalar (complex) visibilities, or 2×2 complex visibility matrices as per the radio interferometer measurement equation (RIME) formalism (Smirnov 2011). Likewise, $\mathcal{I}$ can be treated as a scalar (total intensity) image, or a 2×2 brightness matrix distribution. The derivations below are valid in either case.

We shall use the symbols $\mathbf{u} = (u,v)$ or $\mathbf{u} = (u,v,w)$ to represent baseline coordinates in units of wavelength, and $\mathbf{u}^{\mathrm{m}}$ for units of metres, with $\mathbf{u} = \mathbf{u}^{\mathrm{m}}/\lambda = \mathbf{u}^{\mathrm{m}}\nu/c$.

2.1 Visibility and relation with the sky

An interferometer array measures the quantity $\mathcal{V}(u,v,w)$, known as the visibility function. Here, the coordinates u,v and w are vector components in units of wavelength, describing the distance between antennas p and q, called the *baseline*. The w axis is oriented towards the *phase centre* of the observed field, while u points east and v north. Given a sky distribution $\mathcal{I}_0(l,m)$, where l,m are the direction cosines, the nominal observed visibility is given by the van Cittert-Zernike theorem (Thompson 1999; Thompson et al. 2001) as

$$\mathcal{V}^{\mathrm{nom}}(u,v) = \iint_{lm} \frac{\mathcal{I}_0(l,m)}{\sqrt{1-l^2-m^2}}\,\mathrm{e}^{-2\pi\mathrm{i}\phi(u,v,w)} dl dm, \quad (2)$$

where $\phi(u,v,w) = ul+vm+w(n-1)$, and $n = \sqrt{1-l^2-m^2}$ (the $n-1$ term comes about when fringe stopping is in effect, i.e. when the correlator introduces a compensating delay to ensure $\phi = 0$ at the centre of the field, otherwise the term is simply n).

Given a pair of antennas p and q forming a baseline $\boldsymbol{u}_{pq} = (u_{pq}, v_{pq}, w_{pq})$, and taking into account the *primary beam* patterns $\mathcal{E}_p(l,m)$ and $\mathcal{E}_q(l,m)$ that define the directional sensitivity of the antennas, this becomes

$$\mathcal{V}_{pq}(u,v) = \iint_{lm} \frac{\mathcal{E}_p \mathcal{I}_0 \mathcal{E}_q^H}{\sqrt{1-l^2-m^2}}\,\mathrm{e}^{-2\pi\mathrm{i}\phi(u,v,w)} dl dm. \quad (3)$$

The first term being integrated is the *apparent sky seen by baseline pq*,

$$\mathcal{I}_{pq} = \frac{\mathcal{E}_p \mathcal{I}_0 \mathcal{E}_q^H}{\sqrt{1-l^2-m^2}}, \quad (4)$$

which in general can be variable in time and frequency. For simplicity, let us assume that both the sky and the primary beam are constant (invariant in time and frequency), and

that the primary beam is the same for all stations. All baselines will then see the same apparent sky throughout the measurement process. Let us designate this by $\mathcal{I}$. Assuming a small FoI ($n \to 1$) and/or a coplanar array ($w = 0$), the above equation becomes a simple 2D Fourier transform :

$$\mathcal{V}(u,v) = \iint_{lm} \mathcal{I}\,\mathrm{e}^{-2\pi\mathrm{i}(ul+vm)} dl dm, \quad (5)$$

or in functional form,

$$\mathcal{V} = \mathcal{F}\{\mathcal{I}\}, \quad \mathcal{I} = \mathcal{F}^{-1}\{\mathcal{V}\}. \quad (6)$$

We'll refer to $\mathcal{V}$ as the *ideal* visibility distribution (as opposed to the *measured* distribution, which is corrupted by averaging in the correlator, as we'll explore below).

Note that the effect of the primary beam can alternatively be expressed in terms of a convolution with its Fourier transform, the *aperture illumination function* (AIF) $\mathcal{A}_p(u,v)$. In functional form:

$$\mathcal{V}_{pq} = \mathcal{A}_p \circ \mathcal{V}_{pq}^{\mathrm{nom}} \circ \mathcal{A}_q^H. \quad (7)$$

2.2 Imaging, averaging and convolution

Earth rotation causes the baseline to rotate in time, which we can denote by $\boldsymbol{u}_{pq}^{\mathrm{m}} = \boldsymbol{u}_{pq}^{\mathrm{m}}(t)$. The baseline in units of wavelength can be treated as a function of frequency and time (from this point onwards we shall assume that the sky is constant across the range of frequencies being observed):

$$\boldsymbol{u}_{pq}(t,\nu) = \boldsymbol{u}_{pq}^{\mathrm{m}}(t)\nu/c. \quad (8)$$

This, in turn, allows us to rewrite the visibility in eq. (5) as a per-baseline function of t,ν:

$$V_{pq}(t,\nu) = \iint_{lm} \mathcal{I}\,\mathrm{e}^{-2\pi\mathrm{i}(u_{pq}(t,\nu)l+v_{pq}(t,\nu)m)} dl dm. \quad (9)$$

Synthesis imaging recovers the so-called "dirty image": the inverse Fourier transform of the measured visibility distribution $\mathcal{V}^{\mathrm{M}}$ sampled by a number of baselines pq at discrete time/frequency points. Inverting the Fourier transform produces the dirty image:

$$\mathcal{I}^{\mathrm{D}} = \mathcal{F}^{-1}\{\mathcal{W} \cdot \mathcal{V}^{\mathrm{M}}\}, \quad (10)$$

where $\mathcal{W}$ is the (weighted) sampling function – a "bed-of-nails" function that is non-zero at points where we are sampling a visibility, and zero elsewhere. If $\mathcal{V}^{\mathrm{M}} = \mathcal{V}$, then this can also be expressed as a convolution of the apparent sky by the *point spread function* $\mathcal{P}$:

$$\mathcal{I}^{\mathrm{D}} = \mathcal{P} \circ \mathcal{I}, \quad \mathcal{P} = \mathcal{F}^{-1}\{\mathcal{W}\}. \quad (11)$$

Designating each baseline as pq, and each time/frequency point as t_k, ν_l, we can represent $\mathcal{W}$ by a sum of "single-nail" functions $\mathcal{W}_{pqkl}$:

$$\mathcal{W} = \sum_{pqkl} \mathcal{W}_{pqkl} = \sum_{pqkl} W_{pqkl}\delta_{pqkl}, \quad (12)$$

where δ_{pqkl} is a delta-function shifted to the uv-point being sampled:

$$\delta_{pqkl}(\boldsymbol{u}) = \delta(\boldsymbol{u} - \boldsymbol{u}_{pq}(t_k,\nu_l)) \quad (13)$$

and W_{pqkl} is the associated weight. The Fourier transform being linear, we can rewrite eq. (10) as

$$\mathcal{I}^{\mathrm{D}} = \sum_{pqkl} W_{pqkl} \mathcal{F}^{H}\{\mathcal{V}^{\mathrm{M}}_{pqkl}\}, \qquad (14)$$

where

$$\mathcal{V}^{\mathrm{M}}_{pqkl} = \delta_{pqkl} V^{\mathrm{M}}_{pq}(t_k, \nu_l) \qquad (15)$$

i.e. the visibility distribution corresponding to the single visibility sample $pqkl$. We can further rewrite eq. (10) again as

$$\mathcal{I}^{\mathrm{D}} = \sum_{pqkl} W_{pqkl} \mathcal{F}^{-1}\{\mathcal{V}^{\mathrm{M}}_{pqkl}\}, \qquad (16)$$

which shows that the dirty image $\mathcal{I}^{\mathrm{D}}$ can be seen as a weighted sum of images corresponding to the individual visibility samples $pqkl$ (each such image essentially being a single fringe pattern).

In the ideal case, we would be measuring instantaneous visibility samples, and (assuming no other instrumental corruptions), we would have $\mathcal{V}^{\mathrm{M}} \equiv \mathcal{V}$, with

$$V^{\mathrm{M}}_{pq}(t_k, \nu_l) = \mathcal{V}(\boldsymbol{u}_{pq}(t_k, \nu_l)), \qquad (17)$$

and consequently,

$$\mathcal{V}^{\mathrm{M}}_{pqkl} = \delta_{pqkl} \mathcal{V}, \qquad (18)$$

resulting in what we'll call the *ideal* dirty image $\mathcal{I}^{\mathrm{DI}}$:

$$\mathcal{I}^{\mathrm{DI}} = \sum_{pqkl} W_{pqkl} \mathcal{P}_{pqkl} \circ \mathcal{I}, \quad \mathcal{P}_{pqkl} = \mathcal{F}^{-1}\{\delta_{pqkl}\} \qquad (19)$$

That is, in the ideal case, each term in the weighted sum is equal to the apparent sky $\mathcal{I}$ convolved with a PSF representing a single visibility sample, $\mathcal{P}_{pqkl}$.

However, an actual interferometer is necessarily non-ideal, in that it can only measure the average visibility over a some time-frequency bin given by the *time* and *frequency sampling intervals* $\Delta t, \Delta \nu$, which we'll call the *sampling bin*

$$\mathsf{B}^{[\Delta t \Delta \nu]}_{kl} = \left[t_k - \frac{\Delta t}{2}, t_k + \frac{\Delta t}{2} \right] \times \left[\nu_l - \frac{\Delta \nu}{2}, \nu_l + \frac{\Delta \nu}{2} \right], \; (20)$$

This measurement can be represented by an integration:

$$V^{\mathrm{M}}_{pqkl} = \frac{1}{\Delta t \Delta \nu} \iint_{\mathsf{B}^{[\Delta t \Delta \nu]}_{kl}} \mathcal{V}(\boldsymbol{u}_{pq}(t, \nu)) d\nu dt. \qquad (21)$$

Inverting the relation of eq. (8), we can change variables to express this as an integration over the corresponding bin $\mathsf{B}^{[uv]}_{pqkl}$ in uv-space:

$$V^{\mathrm{M}}_{pqkl} = \frac{1}{\Delta t \Delta \nu} \iint_{\mathsf{B}^{[uv]}_{pqkl}} \mathcal{V}_{pq}(u, v) \left| \frac{\partial(t, \nu)}{\partial(u, v)} \right| du dv, \qquad (22)$$

where $\mathsf{B}^{[uv]}_{pqkl}$ is the corresponding bin in uv-space. Note that the sampling bins in $t\nu$-space are perfectly rectangular and do not depend on baseline (assuming baseline-independent averaging), while the sampling bins in uv-space are elliptical arcs, and do depend on baseline (hence the extra pq index). Assuming a bin small enough that the fringe rate $\partial \boldsymbol{u}/\partial t$ is approximately constant over the bin, we then have

$$V^{\mathrm{M}}_{pqkl} \sim \iint_{\mathsf{B}^{[uv]}_{pqkl}} \mathcal{V}(\boldsymbol{u}) d\boldsymbol{u}, \qquad (23)$$

Now, let us introduce a *normalized boxcar window function*, $\Pi^{[t\nu]}$

$$\Pi^{[t\nu]}(t, \nu) = \begin{cases} \frac{1}{\Delta t \Delta \nu}, & |t| \leqslant \Delta t/2, \; |\nu| \leqslant \Delta \nu/2 \\ 0, & \text{otherwise}, \end{cases} \qquad (24)$$

using which we may re-write eq. (21) as

$$V^{\mathrm{M}}_{pqkl} = \iint_{\infty} \mathcal{V}_{pq}(t, \nu) \Pi^{[t\nu]}(t - t_k, \nu - \nu_l) dt d\nu, \qquad (25)$$

which can also be expressed as a convolution:

$$V^{\mathrm{M}}_{pqkl} = [\mathcal{V}_{pq} \circ \Pi^{[t\nu]}](t_k, \nu_l), \qquad (26)$$

Likewise, eq. (22) can also be rewritten as a convolution in uv-space:

$$V^{\mathrm{M}}_{pqkl} = [\mathcal{V}_{pq} \circ \Pi^{[uv]}_{pqkl}](\boldsymbol{u}_{pq}(t_k, \nu_l)), \qquad (27)$$

where $\Pi^{[uv]}_{pqkl}$ is a boxcar-like window function that corresponds to bin $\mathsf{B}^{[uv]}_{pqkl}$ in uv-space (and also includes the determinant term of eq. 22). This makes it explicit that each averaged visibility is drawn from a convolution of the underlying visibilities with a boxcar-like window function.

Note what eq. (27) does and does not say. It does say that each individual averaged visibility corresponds to convolving the true visibilities by some window function. However, this window function is different for each baseline pq and time/frequency sample t_k, ν_l (which is emphasized by the subscripts to $\Pi^{[uv]}$ in the equations above). Averaging is thus not a "true" convolution, since the convolution kernel changes at every point in the uv-plane. We'll call this process a *pseudo-convolution*, and the kernel being convolved with ($\Pi^{[uv]}_{pqkl}$) an example of a *baseline-dependent window function* (BDWF). In subsequent sections we will explore alternative BDWFs.

In actual fact, a correlator (or an averaging operation in post-processing) deals with averages of discrete and noisy samples, rather than a continuous integration. Ignoring the complexities of correlator implementation, let us cast this process in terms of a simple averaging operation. That is, assume we have a set of *hi-res* or *sampled visibilities* on a high-resolution time/frequency grid t_i, ν_j:

$$V^{\mathrm{S}}_{pqij} = \mathcal{V}_{pq}(t_i, \nu_j) + \mathcal{N}[\sigma^{(\mathrm{s})}_{pqij}], \qquad (28)$$

where $\mathcal{V}_{pq}$ is given by eq. (9), and $\mathcal{N}$ represents the visibility noise term, which is a complex scalar or complex 2×2 matrix with the real and imaginary parts being independently drawn from a zero-mean normal distribution with the indicated r.m.s. (Wrobel & Walker 1999). The noise term is not correlated across samples. The *lo-res* or *averaged* or *resampled* visibilities are then a discrete sum:
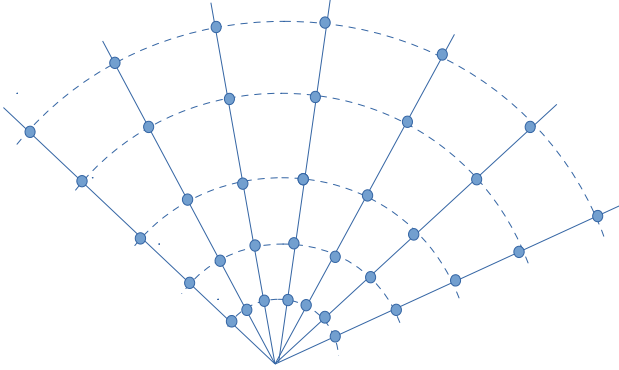
$$V^{\mathrm{M}}_{pqkl} = \frac{1}{n} \sum_{ij \in \mathsf{B}_{kl}} V^{\mathrm{S}}_{pqij}, \qquad (29)$$

where B_{kl} is the set of sample indices ij corresponding to the *resampling bin*, i.e.

$$\mathsf{B}_{kl} = \{ij : \; t_i \nu_j \in \mathsf{B}^{[\Delta t \Delta \nu]}_{kl}\}, \qquad (30)$$

and $n = n_t \times n_\nu$ is the number of samples in the bin. Using the BDWF definitions above, this becomes a conventional discrete convolution (assuming a regular $t\nu$ grid):

$$V^{\mathrm{M}}_{pqkl} = \sum_{i,j=-\infty}^{\infty} V^{\mathrm{S}}_{pqij} \Pi^{[t\nu]}(t_i - t_k, \nu_j - \nu_l). \qquad (31)$$

Figure 1. Schematic of *uv*-coverage for regularly spaced time-frequency samples. Baselines with a longer East-West component sweep out longer tracks between successive integrations.

In *uv*-space, this becomes a discrete convolution on an irregular grid (the $\boldsymbol{u}_{ij}$ grid being schematically illustrated by Fig. 1):

$$V_{pqkl}^{(\mathrm{m})} = \sum_{i,j=-\infty}^{\infty} V_{pqij}^{\mathrm{S}} \Pi_{pqkl}^{[uv]}(\boldsymbol{u}_{ij} - \boldsymbol{u}_{kl}), \qquad (32)$$

2.3 Effect of averaging on the image

In the limit of $\Delta t, \Delta \nu \to 0$, averaging becomes equivalent to sampling. An interferometer must, intrinsically, employ a finitely small averaging interval. The Fourier phase component $2\pi\phi(u,v,w)$ is a function of frequency and time, with increasing variation over the averaging interval for sources far from the phase centre. The average of a complex quantity with a varying phase then effectively "washes out" amplitude, the effect being especially severe for wide FoIs (for an extensive discussion, see Bregman 2012). In the *uv*-plane, this effect is often referred to as *time* and *bandwidth decorrelation*, and *smearing* in the image plane.

The discussion above provides an alternative way to look at decorrelation/smearing. With averaging in effect, the relationship between the measured and the ideal visibility changes to (contrast this to eq. 18):

$$\mathcal{V}_{pqkl}^{\mathrm{M}} = \delta_{pqkl}(\mathcal{V} \circ \Pi_{pqkl}^{[uv]}), \qquad (33)$$

Combining this with eq. 16, and using the Fourier convolution theorem, we can see that the dirty image is formed up as

$$\mathcal{I}^{\mathrm{D}} = \sum_{pqkl} W_{pqkl} \mathcal{P}_{pqkl} \circ (\mathcal{I} \cdot \mathcal{T}_{pqkl}), \qquad (34)$$

with the apparent sky $\mathcal{I}$ now tapered by the baseline-dependent *window response function* $\mathcal{T}_{pqkl}$, the latter being the inverse Fourier transform of the BDWF:

$$\mathcal{T}_{pqkl} = \mathcal{F}^{-1}\{\Pi_{pqkl}^{[uv]}\}. \qquad (35)$$

In other words, the dirty image yielded by averaged visibilities (compare this to the ideal dirty image given by eq. 19) is a weighted average of per-visibility dirty images corresponding to a per-visibility tapered sky. The Fourier transform of a boxcar-like function is a sinc-like function, schematically illustrated in 1-D by Fig. 2(right). Time and bandwidth

smearing represents the average effect of all these individual tapers. Shorter baselines correspond to smaller boxcars and wider tapers, longer baselines to larger boxcars and narrower tapers, and are thus more prone to smearing.

Fig. 3 (produced by simulating a series of high time-frequency resolution observation using MeqTrees(Noordam & Smirnov 2010), and applying averaging) shows the attenuation of a 1 Jy source as a function of distance from phase centre, for a set of different time and frequency intervals. The simulations correspond to JVLA in the C configuration, with an observing frequency of 1.4 GHz. At this frequency, the first null of the primary beam is at $r \approx 36'$, and the half-power point is at $\sim 16'$, thus we can consider the "conventional" FoI (i.e. the half-power beam width, or HPBW) to be about $0.5°$ across. Note that the sensitivity of the upgraded JVLA, as well as improvements in calibration techniques (Perley 2013), allow imaging to be done in the first primary beam sidelobe as well (and in fact it may be necessary for deep pointings, if only to deconvolve and subtract sidelobe sources), so we could also consider an "extended" FoI out to the second null of the primary beam at $r \approx 1.25°$. Whatever definition of the FoI we adopt, Fig. 3 shows that to keep amplitude losses across the FoI to within some acceptable threshold, say 1%, the averaging interval cannot exceed some critical size, say 10s and 1 MHz. Conversely, if we were to adopt an aggressive averaging strategy for the purposes of data compression, say 50s and 5 MHz, the curves indicate that we would suffer substantial amplitude loss towards the edge of the FoI.

Finally, note that the curves corresponding to acceptably low values of smearing across the FoI (i.e. up to 25s and up to 1.25 MHz) have a very gentle slope, with very little suppression of sources *outside* the FoI.

2.4 The case for alternative BDWFs

The window response or image plane response (IPR) function induced by normal averaging (Fig. 2 (right)) is far from ideal: it either suppresses too much within the FoI, or provides limited benefit to suppressing outside the FoI sources, or both. The optimal image plane response would be a disk-like function, unity within the region bounded by a circle and zero outside this region. In 1-D, it is a boxcar-like, as in Fig. 2(left).

The BDWF that would produce such a response is sinc-like, as in 1-D presented in Fig. 2(right). The problem with a sinc is that it has infinite support; applying it over finite-sized bins necessarily means a *truncated* BDWF that results in a suboptimal taper. The problem of optimal filtering has been well studied in signal processing (usually assuming a true convolution rather than the pseudo-convolution we deal with here), and we shall apply these lessons below.

The derivations above make it clear that by using a different BDWF in place of the conventional boxcar-like $\Pi^{[uv]}$ could in principle yield a more optimal tapering response. The obvious catch is a loss in sensitivity. Each visibility sample is subject to an independent Gaussian noise term in the real and imaginary part; the noise of the average of a set of samples is minimized when the average is naturally weighted (or unweighted, if the noise is constant across visibilities). Thus, any deviation from a boxcar F must necessarily increase the noise in the visibilities. Below we will study this
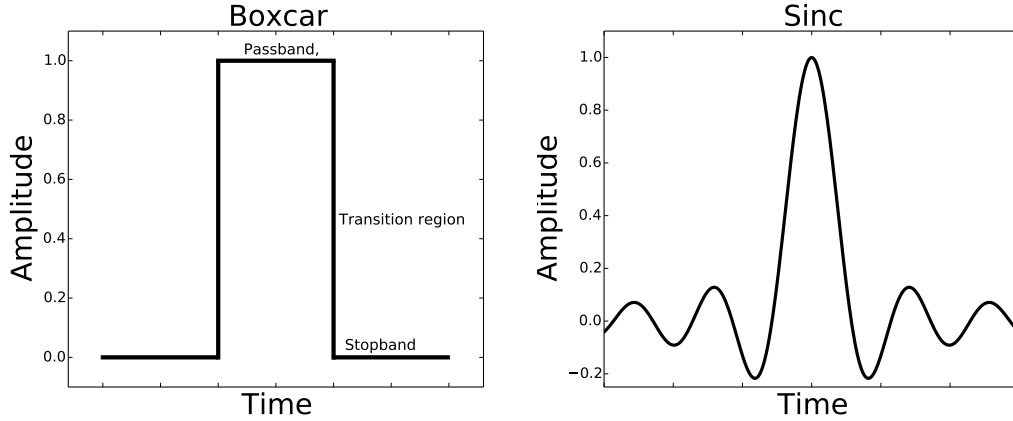
Figure 2. Left: boxcar response. In the uv-plane, this represents the window function corresponding to normal averaging of visibilities. In the image plane, this represents the ideal image-plane response function. Right: Sinc response. In the image plane, this represents the window response function corresponding to a boxcar window function in the uv-plane. In the uv-plane, this represents the ideal window function.
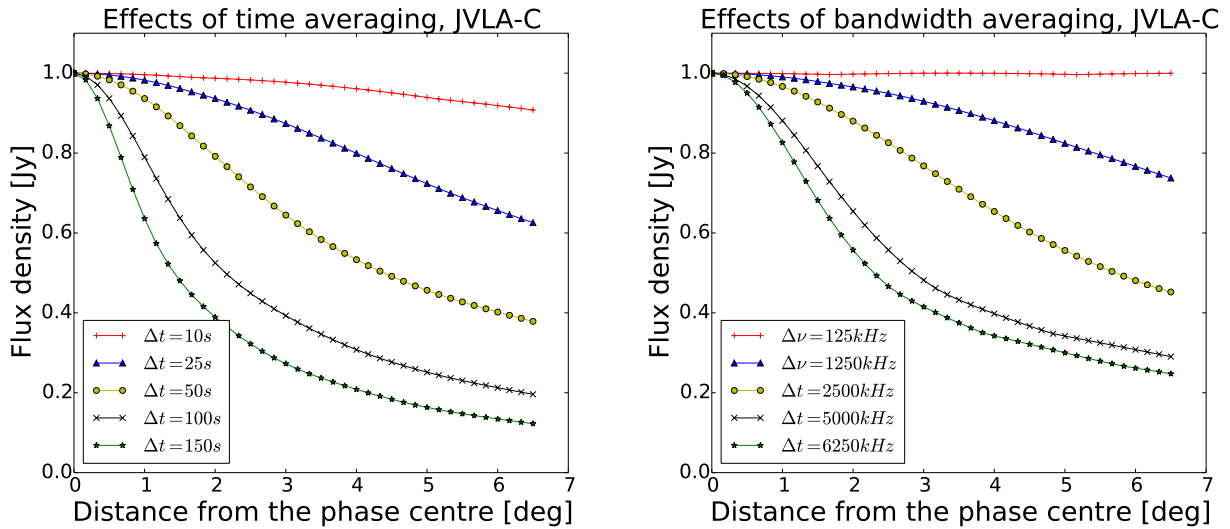
Figure 3. Effects of time and frequency averaging: the apparent intensity of a 1 Jy source, as seen by JVLA-C at 1.4 GHz, as a function of distance from phase centre. (Left) Frequency interval fixed at 125 kHz, time interval varies; (right) time interval fixed at 1s, frequency interval varies.

effect both theoretically and via simulations, to establish whether this trade-off is sensible, and under which conditions.

3   BDWF RELATIONSHIP TO DIGITAL SIGNAL PROCESSING

This work is an specific application of signal conditioning using digital signal processing (DSP). It is useful to relate this work to DSP concepts and terminology.

Ideally, all spatial modes, up to the resolution of the longest baseline, are sampled in a the 2-D continuous sky image $\mathcal{I}$. That requires Nyquist sampling the visibility domain out to the longest baseline spatial modes. This is rarely possible due to the unfilled holes in the uv coverage during an observation, the lower spatial frequency cut-off due to physical element limitations, and sampling bias in the low spatial frequency region of the visibility plane compared to higher spatial frequencies due to baseline distribution. For a fixed time length a long baseline will cover a longer track in visibility space compared to a shorter baseline which results in the lower spatial modes being oversampled compared to higher spatial modes. On shorter baselines the window functions act as filters with a larger noise equivalent bandwidth compared to longer baselines. This necessitates the use of baseline-dependent window functions to optimize the image plane response (IPR), which is the aggregate spectral response of the combined individual baseline filters.

A matched filter maximizes the signal-to-noise of a desired signal in the presence of noise. In the case of synthesis imaging the desired signal is within a defined FoI on the

Sinc Filter Response
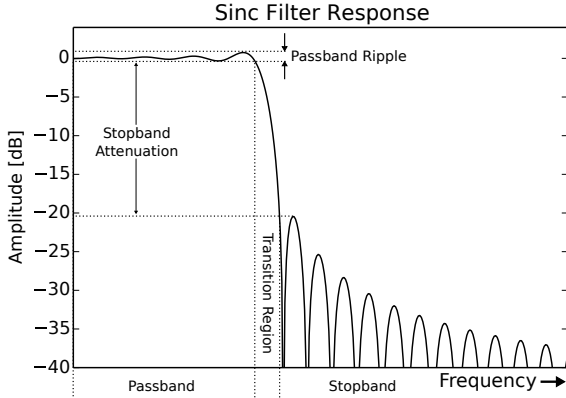
Figure 4. Response of a Sinc filter window. A filter response is segmented into three regions: passband, stopband, and transition region. Filter design can optimize for various metrics such as the peak sidelobe level (PSL), sidelobe rolloff rate (SLR), passband ripple, etc.

sky. This is the passband region of the IPR and sky signal outside of this FoI is in the stop band which we would like to suppress. The choice of BDWF can depend on the requirement to limit the transition width between the pass and stop band or limit the pass band ripple, or minimize the sidelobe level or some other filter optimization metric. An approximate matched filter will be an array, sky field, and observation dependent filter.

Eq. (29) is a decimation operation, the choice of window size is a compromise which uses the largest possible window size that does not introduce significant smearing. The window size could not be defined analytically, given that it depends on the FoI we want to achieve, the interferometer array layout, the observation frequency, and baselines length and directions.

Confusion in terminology can arise due to the number of different signal domains used in this work. The visibility of a baseline is sampled constantly in the correlator time domain, but is irregularly sampled in the 2-D visibility domain (for simplicity we are only analyzing the uv-plane of the 3-d uvw-space). The imaging domain is the 2-D Fourier pair of the visibility space. In synthesis imaging we are making the assumption that the sky is a constant signal but a time vary signal is measured due to the array rotation (usually due to the Earth) with respect to the observed field. But, this application is not a linear time-invariant system which leads to complexity in the analysis of the signal conditioning. The window function filters are linear but are dependent on baseline length which varies with time. It is not sufficient to just analyze the filter impulse response. Instead, for our analysis we will use the aggregate image plane response.

For this work we have chosen to use Sinc and Bessel window functions. Figure 4 is the generic response of a Sinc function, we use the standard DSP filter terminology to describe the IPR of visibility domain window functions. To construct a 2-D Sinc and Bessel from 1-D, we will use the following definitions:

$$S(u, v) = S(u)S(v),$$
$$J_0(u, v) = J_0(r), \quad r = \sqrt{u^2 + v^2}.$$

where S and J_0 are the sinc window and Bessel function of the first kind of order zero (Watson 1995) respectively. Appendix A provides a review of these window functions along with common 1-D window functions which were also considered. This work does not attempt to find the optimal matched filter, we leave this to future work. All the BDWF presented are finite impulse response (FIR) filters followed by decimation. That is, they are window-function-weighted, moving averages of the measured visibilities. In the simple case of non-overlapping windows the decimation rate is equal to the size of the window filter. The overlapping window filters presented in Section 4.1 can be seen as a type of polyphase filter. We do not explore the use of infinite impulse response (IIR) filters in this work, but this is a clear path for further study.

4 APPLYING WINDOW FUNCTIONS TO VISIBILITIES

While visibilities are (usually) regularly sampled in $t\nu$-space, in uv^{m}-space this is not so. In frequency, the sampling positions go as $\sim \lambda^{-1}$, while in time, baselines with a longer East-West component sweep out longer tracks between successive integrations (Fig. 1). Applying a window function with a constant integration window in $t\nu$ space corresponds to different-sized windows in uv-space. In the case of normal averaging, this results in the boxcar-like window $\Pi^{[uv]}$ of eq. (27) having a baseline-dependent scale. The scale of the tapering response being inversely proportional to the scale of the window function, this results in more decorrelation (i.e. a narrower achievable FoI) on longer baselines.

By defining our alternative window functions in uv-space (in units of wavelength), we can attempt to "even out" the decorrelation response across baselines. For a given BDWF $X(u, v)$, we have the following recipe for computing resampled visibilities (compare to eq. 32):

$$V_{pqkl}^{(\mathrm{m})} = \frac{\sum\limits_{i,j \in \mathsf{B}_{kl}} V_{pqij}^{\mathrm{S}} X(\boldsymbol{u}_{pqij} - \boldsymbol{u}_{pqkl})}{\sum\limits_{i,j \in \mathsf{B}_{kl}} X(\boldsymbol{u}_{pqij} - \boldsymbol{u}_{pqkl})}, \qquad (36)$$

where $\boldsymbol{u}_{pqkl}$ is the midpoint of the resampling bin B_{kl} in uv-space. The main lobe of the window function then has the same scale across the entire uv-plane, while the resampling bins have different uv-sizes. Conversely, in $t\nu$-space the bins are regular, while the main lobe of the effective window function scales inversely with the baseline fringe rate. Furthermore, the window function is truncated at the edge of each bin; on the shortest baselines this truncation is extreme to the point of approaching the boxcar-like $\Pi^{[uv]}$ (Fig. 5).

The downside of this simple approach is twofold. Firstly, while all of the window functions above nominally exhibit far lower sidelobes than the boxcar (i.e. more suppression for out-of-FoI sources), they no longer perform that well under truncation, with extremely truncated window functions at the shorter baselines becoming boxcar-like. Secondly, taking a weighted sum in eq. 36 increases the noise in comparison to normal averaging.
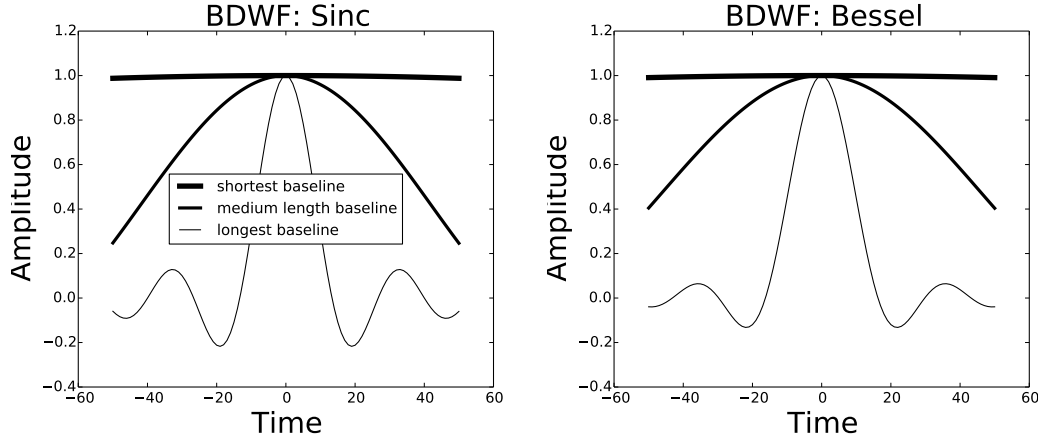
Figure 5. Cross-sections through two different BDWFs (left: sinc, right: Bessel) defined in uv-space, plotted along the time axis. This shows that the effective window function is a scaling and truncation of the underlying window function, with the shortest baselines reducing to a boxcar-like window function.
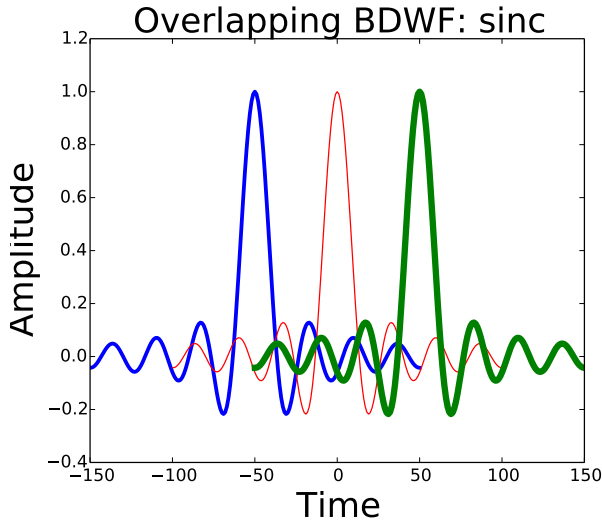
Figure 6. Overlapping BDWFs representing adjacent resampling bins. This corresponds to overlap factor $\alpha = 3$ in time.

4.1 Overlapping BDWFs

A more sophisticated approach involves overlapping BD-WFs. Normal averaging implicitly assumes that the resampling bins B_{kl} in eq. (36) don't overlap for adjacent kl, since they represent adjacent averaging intervals. There is, however, no reason (apart from computational load) why we cannot take the sum in eq. (36) over larger bins. Let us define the *window bin* for *overlap factors* of α, β as

$$B_{kl}^{[\alpha\beta]} = \left\{ ij : \ t_i\nu_j \in B_{kl}^{[\alpha\Delta t, \beta\Delta\nu]} \right\}, \qquad (37)$$

i.e. as the set of sample indices corresponding to a bin of size $\alpha\Delta t \times \beta\Delta\nu$ in $t\nu$-space. Let us then compute the sums in eq. (36) over the window bin. This becomes distinct from the resampling bin: while the latter represents the spacing of the resampled visibilities, the former represents the size of the window over which the convolution is computed. Only for $\alpha = \beta = 1$ do the two bins become the same.

Overlapping BDWFs are schematically illustrated in

Fig. 6. For normal averaging overlapping offers no benefit, since it only broadens $\Pi^{[uv]}$ and therefore increases smearing. But for a well-behaved BDWF, enlarging the window bin (while maintaining the same window function scale) means less truncation – thus lower sidelobes – and decreased noise, as more sampled visibilities are taken into account.

To distinguish overlapping BDWFs from non-overlapping ones, in the rest of the paper we will designate the window functions employed as WF-$\alpha\times\beta$. For example, sinc-3×2, J_0-1×1 (i.e. no overlap), etc. If resampling is only done in one direction (only time or only frequency), we'll indicate this as e.g. J_0-3×−.

4.2 Noise penalty estimates: analytic

Let us now work out analytically the *noise penalty* associated with replacing an unweighted average by a weighted sum. For simplicity, let's assume that the noise term has constant r.m.s. σ_s across all baselines and samples. If the resampling bin consists of $n_{\mathrm{avg}} = n_t \times n_\nu$ samples, and since the noise is not correlated between samples, the noise on the averaged visibilities in eq. (29) will be given by

$$\sigma_{\mathrm{m}}^2 = \frac{1}{n_{\mathrm{avg}}^2} \sum_{i=1}^{n_{\mathrm{avg}}} \sigma_s^2 = \frac{\sigma_s^2}{n_{\mathrm{avg}}} \qquad (38)$$

Note that the noise is uncorrelated across averaged visibilities. We can therefore use the the imaging equation (16) to derive the following expression for the variance of the noise term in each pixel of the dirty image:

$$\sigma_{\mathrm{pix}}^2 = \frac{(\sum_{pqkl} W_{pqkl}^2 \sigma_{\mathrm{m}}^2)}{(\sum_{pqkl} W_{pqkl})^2}, \qquad (39)$$

which for natural image weighting ($W \sim \sigma_{\mathrm{m}}^{-1}$, i.e. $W \equiv 1$ in this case) is simply

$$\sigma_{\mathrm{pix}}^2 = \frac{1}{N}\frac{\sigma_s^2}{n_{\mathrm{avg}}}, \qquad (40)$$

where N is the total number of visibilities used for the synthesis.

To simplify further notation, let's replace *pqkl* by a single index μ, enumerating all the lo-res visibilities $V_\mu^{\rm M}$, with $\mu = 1 \ldots N$. If we now employ eq. (36) to compute the lo-res visibilities using some BDWF $X(u,v)$, the noise term becomes different per each visibility μ:

$$\sigma_{X\mu}^2 = \frac{\sum X^2(\boldsymbol{u}_{pqij} - \boldsymbol{u}_{pqkl})}{\left[\sum X(\boldsymbol{u}_{pqij} - \boldsymbol{u}_{pqkl})\right]^2} \sigma_{\rm s}^2 \qquad (41)$$

where both sums are taken over the window bin, $i, j \in \mathsf{B}_{kl}$. Let us define the *visibility noise penalty* associated with BDWF X and visibility μ as the relative increase in noise over the unweighted average, i.e.

$$\Xi_{X\mu} = \frac{\sigma_{X\mu}}{\sigma_{\rm m}} = \frac{\sqrt{n_{\rm avg} \sum X^2(\boldsymbol{u}_{pqij} - \boldsymbol{u}_{pqkl})}}{\sum X(\boldsymbol{u}_{pqij} - \boldsymbol{u}_{pqkl})}. \qquad (42)$$

Note that in the case of overlapping BDWFs, the window bin in eq. 41 is larger than the resampling bin, and contains n_X samples, with $n_X = \alpha\beta n_{\rm avg}$, where α and β are the overlap factors. For $\alpha = \beta = 1$, it is easy to see that $\Xi_{X\mu} \geqslant 1$, and only reaches 1 when $X \equiv 1$. In other words, non-overlapping BDWFs always result in a visibility noise penalty above 1, while overlapping BDWFs can actually *reduce* noise in the resampled visibilities.

While paradoxical at first glance, this reduction in noise does **not** result in a net gain in image sensitivity. The reason for this is that with overlap in effect, the noise terms become correlated across resampled visibilities *kl* (within the same baseline *pq*), with each hi-res visibility sample contributing to multiple resampled visibilities, and the image noise term no longer follows eq. (39).

If the resampled visibilities correspond to a single-channel snapshot, or if the BDWFs are non-overlapping, then the noise across visibilities remains uncorrelated, and we can compute the *image noise penalty* associated with imaging weights W and BDWF X as

$$\Xi_X^W = \frac{\sigma_{\rm pix, X}^2}{\sigma_{\rm pix}} = \frac{n}{\sigma_{\rm s}} \frac{(\sum_\mu W_\mu^2 \sigma_\mu^2)}{(\sum_\mu W_\mu)^2} = \frac{(\sum_\mu W_\mu^2 \Xi_{X\mu}^2)}{(\sum_\mu W_\mu)^2} \qquad (43)$$

In the case of natural weighting ($W_\mu = \sigma_\mu^{-1}$) this reduces to:

$$\Xi_X^{\rm nat} = \frac{N}{\sum_\mu \Xi_{X\mu}^{-1}}. \qquad (44)$$

4.3 Noise penalty estimates: empirical

In this section we employ simulations to empirically verify noise estimates computed using the derivation above. We generate a high resolution ("high-res") JVLA-C measurement set (MS) corresponding to a 400s synthesis with 1s integration, with 30 MHz of bandwidth centred on 1.4 GHz, divided into 360 channels of 83.4 kHz each. The MS is filled with simulated thermal noise with $\sigma_{\rm s} = 1$ Jy. We then generate a low resolution ("low-resolution") MS using 100s integration, with a single frequency channel of 10 MHz. This MS receives the resampled visibilities. The size of the resampling bin is thus 100s by 10MHz, or 100×120 in terms of the number of hi-res samples.

We then resample the hi-res visibilities using a number of BDWFs, and store the results in the lo-res MS:

• Standard averaging to 100s and 10MHz (using the middle 120 channels). This gives us the baseline noise estimate.

BDWF	Ξ analytic	Ξ sim
sinc-1×1	1.247	1.22
sinc-4×3	1.242	1.20
besse-1×1	1.178	1.16
bessel-4×3	1.109	1.12

Table 1. A comparison of image noise penalties associated with different BDWFs, computed analytically vs. simulations.

• Sinc and Bessel windows using the same bin, without an overlap, tuned to a FoI of $2°$.
• The same windows with overlap factors of 4×3.

We then image the lo-res MS and take the r.m.s. pixel noise across the image as an estimator of $\sigma_{\rm pix}$, divide it by the baseline estimate produced with normal averaging, and compare the resulting noise penalty with that predicted by eq. 44. Note that this estimator is not perfect, since image noise is correlated across pixels. Nonetheless, we obtain results that are broadly consistent with analytical predictions (Table 1).

Fig. 7 shows the predicted visibility noise penalty for the same BDWFs, as a function of East-West baseline component, which determines the baseline rotation speed. Note that the noise penalty rises sharply towards longer E-W baselines. Note also that the penalty is well below 1 on shorter baselines, when overlapping is in effect.

5 SIMULATIONS AND RESULTS

In this section we use BDWFs to resample simulated visibility data, and study the effect on smearing and source suppression. Apart from a few examples documented separately, the basis interferometer configuration employed in the simulations corresponds to JVLA-C observing at 1.4 GHz. Similarly to Sect. 4.3, we create a "high-res" measurement set corresponding to a 400s synthesis at 1s integration, with 30 MHz total bandwidth centred on 1.4 GHz, divided into 360 channels of 83.4 kHz each. The MS is populated by noise-free simulated visibilities corresponding to a single point source at a given distance from the phase centre. We then generate "low-res" MSs to receive the resampled visibilities, resample the latter using a range of BDWFs, convert the visibilities to dirty images (using natural weighting unless otherwise stated), and measure the peak source flux in each image. Since each dirty image corresponds to a single source, the peak flux gives us the degree of smearing associated with a given BDWF and sampling interval.

For the first set of simulations, the "low-res" MSs correspond to a 100s and 10MHz synthesis. We employ three sampling rates, 25s×2.5MHz, 50s×5MHz and 100s×10MHz (thus 4 timeslots and 4 channels, 2 timeslots and 2 channels, and single-channel snapshot).

A typical performance comparison for the JVLA-C configuration at 1.4 GHz is given by Fig. 8. This figure illustrates some of the principal achievements of the present work, so let us spend some time explaining it. The horizontal axis represents distance from phase centre, while the vertical axis of the left-hand plot represents the degree of smearing (left plot). Unity corresponds to no smearing; this is the case at phase centre, thus all curves start at unity. The three thick gray curves correspond to normal averaging into
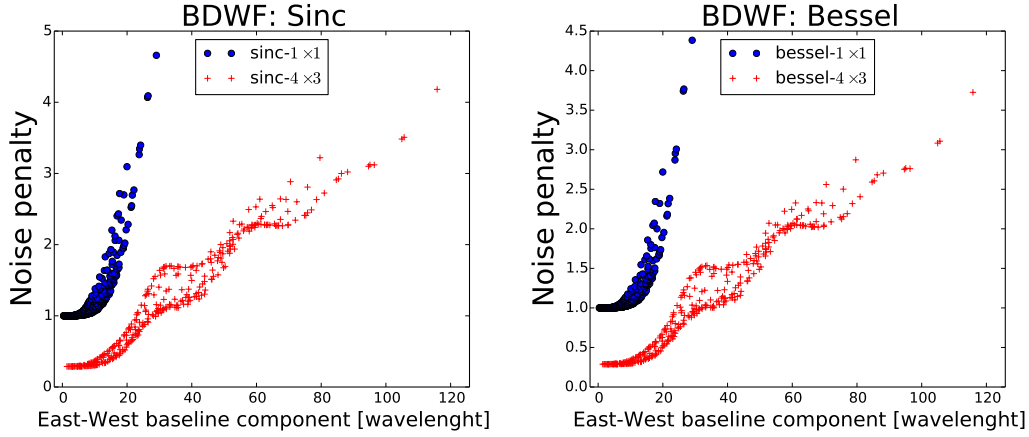
Figure 7. Noise penalty w.r.t. normal averaging as a function of baseline length for two different BDWFs (sinc and Bessel), with and without overlap. JVLA-C, 1.4 GHz, sampling intervals of 100s and 10 MHz.
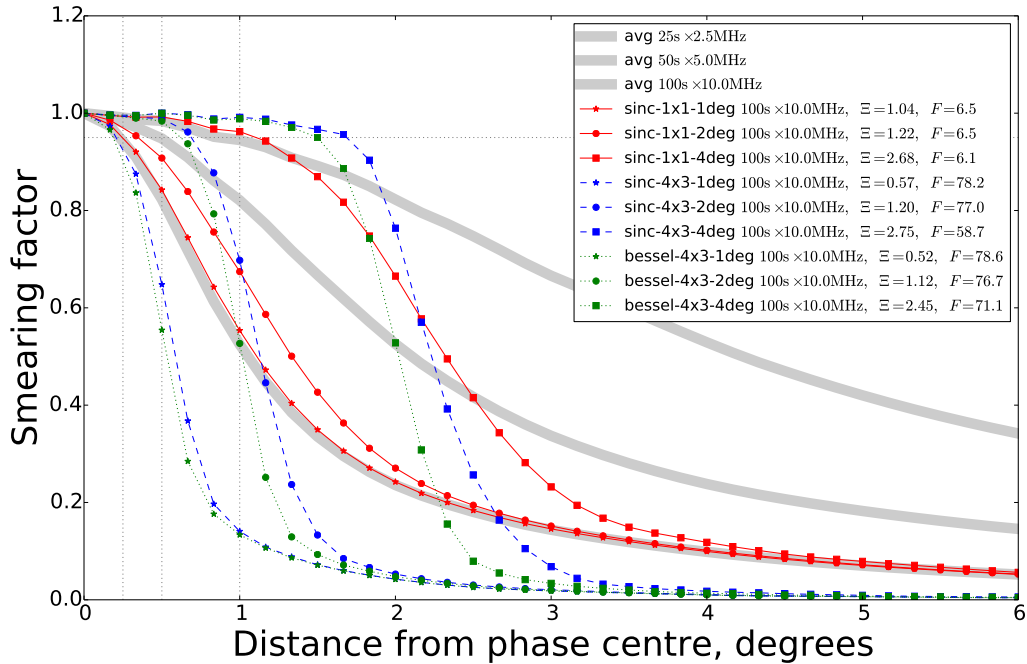
Figure 8. JVLA-C 1.4 GHz. Smearing as a function of distance from phase centre, for conventional averaging with 25s×2.5MHz, 50s×5MHz and 100s×10MHz bins, and for several BDWFs with 100s×10MHz bins. The noise penalty Ξ and the far-source suppression factor F are given relative to 25s×2.5MHz averaging.

25s×2.5MHz, 50s×5MHz and 100s×10MHz. We can (rather arbitrarily) define a series of "acceptable" smearing levels by specifying a FoI radius, and the maximum extent of smearing over that FoI. For the FoI radius, we may pick e.g. the half-power point of the primary beam, the main lobe of the primary beam, or extent of the first sidelobe of the primary beam. For JVLA's 25m dishes at this frequency, these radius correspond to ∼ 0.25°, 0.5°, and 1°, respectively; they are indicated by thin vertical lines in the figure. The thin horizontal line indicates our chosen smearing threshold of 0.95.

In the right plot, all the curves are normalized with respect to the 25s×2.5MHz averaging curve.

For regular averaging, the three chosen bin sizes happen to roughly correspond to acceptable levels of smearing over the three chosen FoI values. The other curves show the performance of a few different BDWFs, all at 100s×10MHz sampling. There are three types of BDWFs shown, indicated by line style (and colour, in the colour version of the plot):

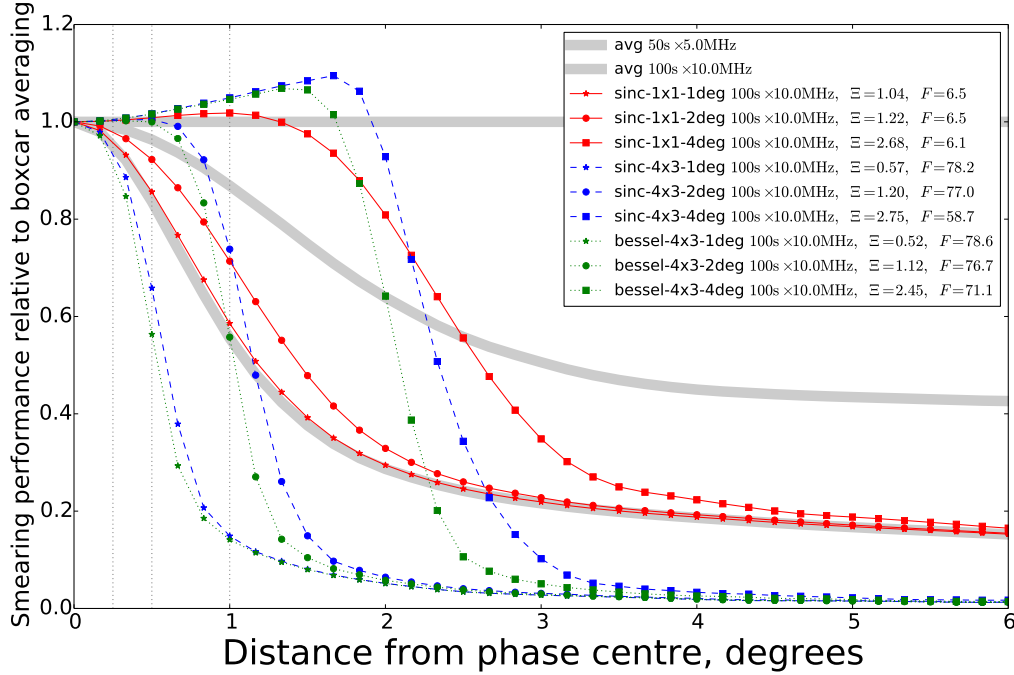sinc-1×1 i.e. a non-overlapping sinc window (solid line, red)

Figure 9. JVLA-C 1.4 GHz. Results of Fig. 8 normalized to the 25s×2.5MHz averaging curve.

sinc-4×3 i.e. an overlapping sinc window (dashed line, blue)

bessel-4×3 i.e. an overlapping Bessel window (dotted line, green)

These are tuned to three different FoI settings, as indicated by the plot symbol: 1° (star), 2° (circle), 4° (square).

The plot is meant to show performance of BDWFs at 100s×10MHz versus a "baseline case" of 25s×2.5MHz averaging, the latter being an acceptable averaging setting for this particular frequency and telescope geometry. The legend next to the plot therefore indicates Ξ, the noise penalty associated with that particular BDWF, and F, the far source suppression factor. Both values are calculated w.r.t. the baseline case. Note the following salient features:

• All overlapping BDWFs provide outstanding far source suppression in this regime, with F in the $60 \sim 80$ range. The non-overlapping sinc (solid red lines) only achieves F 6, which is similar to regular averaging at the same rate.

• Noise performance is excellent for the 1° BDWFs. There is a small noise penalty at 2°, and a larger (over a factor of 2) noise penalty at 4°. This can be easily understood by considering the shape of BDFWs as a function of FoI: smaller FoIs correspond to broader windows that become more "boxcar-like" over the sampling interval, and vice versa. This means that, in this particular configuration, BDWFs cannot achieve a FoI of 4° at 10s×100MHz without a substantial sacrifice in sensitivity. We shall return to this issue below.

• If the desired FoI size is $r \sim 0.5 - 1°$, overlapping BDWFs (sinc-4x3-2deg and bessel- 4x3-2deg) provide excellent performance at 100s×10MHz. Compared to averaging at 25s×2.5MHz, they achieve a factor of 16 data compres-

sion with minimal loss of sensitivity, with excellent tapering behaviour: the smearing performance across the FoI is equivalent to (or better) than that of normal averaging, and out-of-FoI source suppression is almost two orders of magnitude higher.

Fig. 9 presents the same results in an alternative way. Here, the recovered flux is shown relative to the baseline case of 25s×2.5MHz averaging. This clearly illustrates the excellent performance of overlapping BDWFs tuned to 2°.

5.1 Noise penalties and overlapping BDWFs

Values of $\Xi < 1$ above may be paradoxical at first, since one can't theoretically exceed the noise performance of the unweighted average. This, however, is an artefact of our short simulation. Overlapping BDWFs are essentially averaging in "bonus signal" from regions of overlap extending outside the nominal time and frequency coverage. In our case, at 100s×10MHz sampling, a BDWF with 4×3 overlap is actually adding up signal over a 400s×30MHz bin, i.e. a bin that is a factor of 12 larger (though of course the bonus sensitivity thus gained is much less than the theoretically available $\sqrt{12}$, since the weights over the overlap regions correspond to the "wings" of the window function, and are thus small). This can easily result in lower per-visibility noise than that achieved by regular averaging over 100s×10MHz, and correspondingly higher snapshot sensitivity.

In the more realistic case of a long, multiple-channel synthesis (what we'll call a *full synthesis*), the effects of bonus sensitivity disappear. While the noise on individual visibilities remains nominally lower in a full synthesis thanks to the overlap, it becomes correlated across neighboring

uv-bins, so there is no net gain in image-plane sensitivity. Strictly speaking, at the "edge" of the synthesis, overlapping BDWFs are still pulling in some bonus signal from overlap regions extending beyond the synthesis coverage, but since the area of this overlap is negligible compared to the coverage of the full synthesis, so is the effect of the bonus signal.

In other words, simulating a snapshot observation results in underestimated noise penalties, compared to the real-life case of a full synthesis. We should expect the noise penalties to go up (and eventually exceed unity) as we increase the synthesis time and number of channels. Fig. 10 presents the results of such a simulation. This shows a a 1800s×200MHz synthesis, sampled at the same rates as above. The results should be compared to and contrasted with those of Fig. 8. Note that the tapering response of BDWFs is nearly identical, while the noise penalties are indeed higher. With 4×3 overlap and 100s×10MHz sampling, the total signal accessed by overlapping BDWFs corresponds to 2100s×220MHz, which gives a theoretical maximum of a factor of ~ 1.13 in bonus sensitivity. In other words, the values of Ξ in Fig. 10 are still underestimated, but by 13% at most (which explains $\Xi < 1$ for the 1° case). From this we may safely extrapolate that the noise penalty of BDWFs matched to $1-2°$ FoIs will remain reasonable even for a much longer and wider band synthesis.

5.2   FoIs and sampling rates

For BDWFs, a given FoI tuning represents a characteristic scale in the uv-plane, which is inversely proportional to the FoI parameter. On the other hand, the uv-bin sampled by any given visibility is proportional to the integration time, fractional bandwidth, and baseline length. Since the window function is truncated at edge of the averaging bin (which can be larger by the sampling bin by a factor of several, if overlapping BDWFs are employed), there is, for any given baseline, some kind of optimal range of uv-bin sizes over which BDWFs tuned to a particular FoI setting are "efficient". Over smaller bins, BDWFs become equivalent to a boxcar averaging, over larger bins, BDWFs penalize too much sensitivity as they down-weigh more samples. Since this optimal bin size is proportional to baseline length, the overall optimum is dependent on the distribution of baselines in the array.

Furthermore, the sampling rate needs to be "balanced" in time and frequency for BDWFs to achieve efficient tapering response. If the uv-bins are elongated, the window function becomes truncated (i.e. more boxcar-like) across the bin, which reduces its ability to induce the desired taper. Since the orientation of the bins changes as the baseline rotates, the cumulative effect is an average degradation of the tapering response, in the sense that it becomes closer to that of boxcar averaging. In this sense, the optimal uv-bin shape is square-like. This occurs when the fractional bandwidth is equal to the arc section swept out by the baseline over one bin. For a polar observation (circular uv-tracks), we can express this as

$$\Delta\nu/\nu = 2\pi(B_x/B)(\Delta t/24\text{h}), \qquad (45)$$

where B is the baseline length, and B_x is its East-West component. Rewriting this in terms of more convenient units, we

end up with

$$\frac{\Delta\nu_{\text{MHz}}}{\Delta t_{\text{s}}} \approx \frac{\nu_{\text{MHz}}}{14000} \cdot \frac{B_x}{B}, \qquad (46)$$

leading to a simple rule-of-thumb: at 1.4 GHz, an East-West baseline sweeps out a square-like bin when the integration time in seconds is 10 times the channel width in MHz (hence the use of bin sizes such as 100s×10MHz in the analysis here).

The interaction between uv-bin size and tapering response is illustarted by Fig. 11. Here we compare the performance of two BDWFs tuned to a 4° FoI – a non-overlapping sinc-1×1 filter (solid red lines) and an overlapping sinc-4×3 filter (dashed blue lines) – over three sampling bin sizes: 25s×2.5MHz, 50s×5MHz and 100s×10MHz. For reference, the performance of boxcar averaging over the same bin sizes is indicated by the thick grey lines. Note how at the smaller bin size, the non-overlapping sinc is practically equivalent to a boxcar in terms of tapering response; at the larger bin size, it begins to shape the FoI. Introducing an overlap improves the response considerably. An overlapping filter at 25s×2.5MHz achieves almost the same tapering response as a non-overlapping one at 100s×10MHz (which is not surprising, if one considers that the effective averaging bin size in the former case is 100s×7.5MHz). However, for all filters, at 100s×10MHz the noise penalty goes up quite sharply.

This illustrates that 50s×5MHz is an appropriate BDWF sampling rate for achieving a 4° FoI (for JVLA-C configuration at 1.4 Ghz), providing a reasonable trade-off between tapering response and noise penalty. At higher sampling rates, the tapering response is degraded, while at lower sampling rates, the noise penalty increases. In comparison (as we saw in the previous section), for FoIs of $1-2°$, BDWFs achieve a good trade-off at 100s×10MHz sampling.

It is interesting to consider how optimal BDWF sampling changes as a function of array size. Fig. 12 shows a simulation for JVLA-C at 14 GHz. (Since our results are completely determined by uv-plane geometry in wavelengths, this is equivalent to JVLA-C scaled up by a factor of 10 at an observing frequency of 1.4 GHz). From Eq. 46, we can see that square-like uv-bins correspond to sampling rate combinations such as 10s×10MHz. The simulation presented here is for a 1800s×200MHz synthesis, i.e. is closer to the full synthesis rather than a snapshot case. Comparing Figs. 12 and 10, we find nearly identical BDWF performance (in terms of tapering response and noise penalty) at 14 GHz and 1.4 GHz, with only the optimal sampling rate being different.

5.3   BDWFs for wide-field VLBI

In the VLBI case, it is usually a combination of smearing and data rates, rather than the primary beam, that effectively limits the FoI. For example, the current European VLBI Network (EVN) correlator (Keimpema et al. 2015) operated by the Joint Institute for VLBI in Europe (JIVE) is capable of producing data at dump rates down to 10ms, with 16 MHz of total bandwidth split into up to 8192 channels. The maximum available FoI of an EVN experiment is restricted by the smallest primary beam, which is usually that of the 100m Effelsberg telescope – or about 10′ in diameter at L-
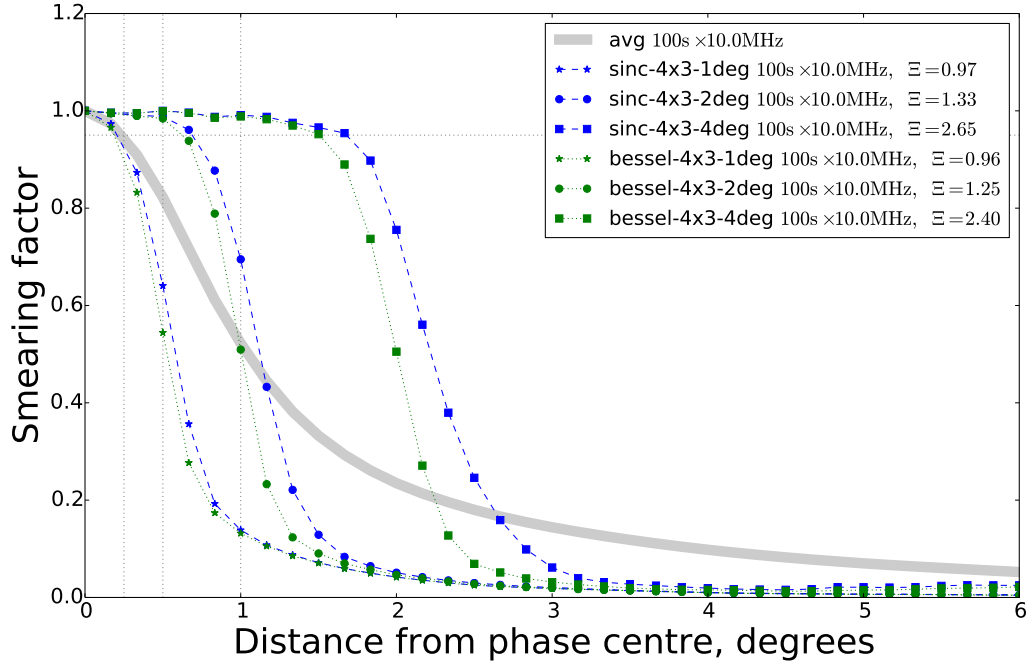
Figure 10. JVLA-C 1.4 GHz, long wideband synthesis. Smearing as a function of distance from phase centre, for conventional averaging with 100s×10MHz bins, and for overlapping BDWFs with 100s×10MHz bins. The noise penalty Ξ is given relative to 100s×10MHz averaging.
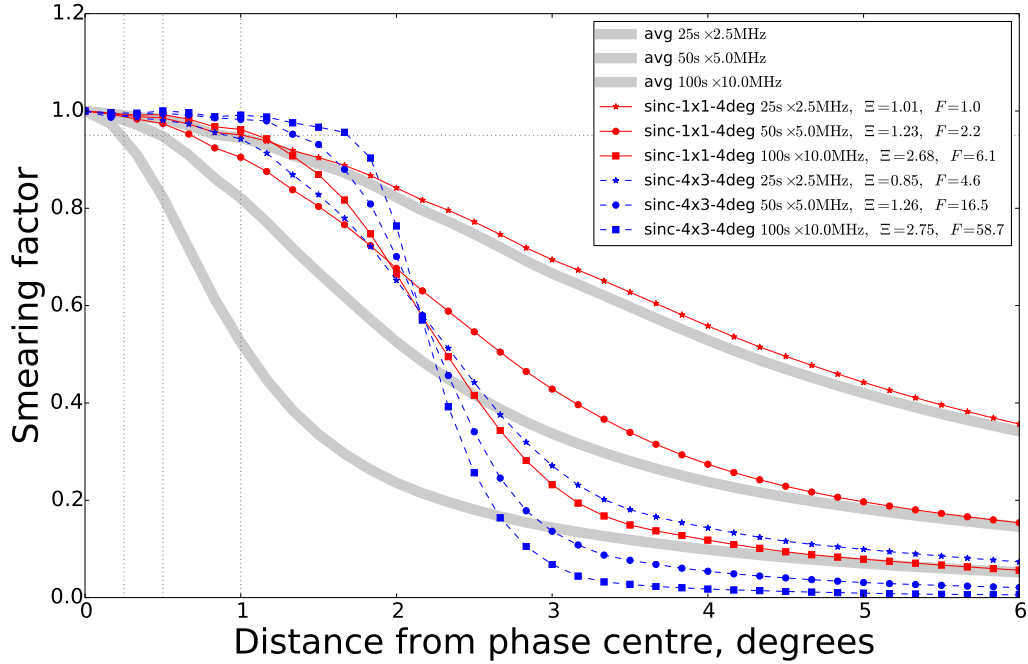
Figure 11. JVLA-C 1.4 GHz. Smearing as a function of distance from phase centre, for conventional averaging with 25s×2.5MHz, 50s×5MHz and 100s×10MHz bins, and for several BDWFs with 100s×10MHz bins. The noise penalty Ξ and the far-source suppression factor F are given relative to 25s×2.5MHz averaging.
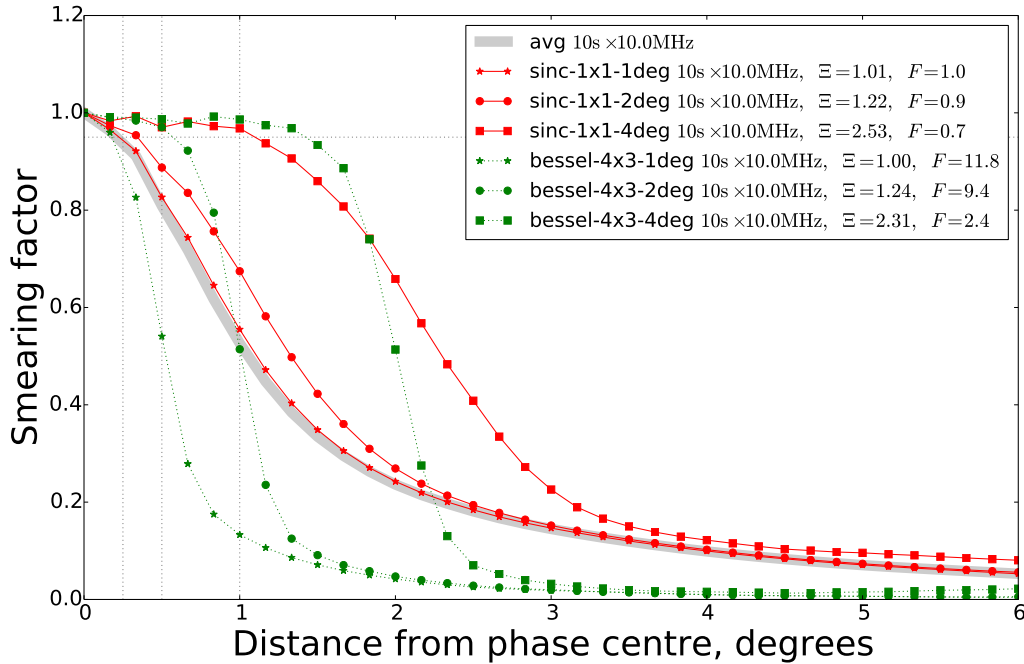
Figure 12. JVLA-C 14 GHz. Smearing as a function of distance from phase centre, for conventional averaging with 2.5s×2.5MHz, 5s×5MHz and 10s×10MHz bins, and for several BDWFs with 10s×10MHz bins. The noise penalty Ξ and the far-source suppression factor F are given relative to 2.5s×2.5MHz averaging.

band. The ENV calculator[2] shows that a dump rate of 0.125s and 1024 channels (16 kHz) is required to keep smearing to within 10% across this FoI. Due to the large computational and storage requirements, such data rates have only been employed in one-off experiments. For routine use, techniques such as multiple-phase centre correlation are more common. Typically, data is averaged into more modest sampling rates of 2s and 32 channels. This restricts the effective (L-band) FoI to about 20″, and thus limits the scientific usefulness of archival data to narrow-FoI experiments.

In this section we investigate whether the use of BD-WFs can enable true wide-field VLBI. We simulate a 1.6 GHz EVN observation employing eight stations (Effelsberg, Hartebeesthoek, Jodrell Bank, Noto, Onsala, Torun, JVLA, Westerbork, Shanghai), with a maximum baseline of 10161km. Fig. 13 compares the smearing response of normal averaging to that of two overlapping Bessel BDWFs, employing 0.5s and 25 kHz sampling. At these data rates, it becomes almost practical to have a full-FoI EVN archive.

For comparison, we also show the performance of BD-WFs for a hypothetical fast-transient archive application. In order to localize potential fast radio bursts (FRBs), we would need to retain a high time resolution of 10ms, as well as a lower spectral resolution for de-dispersion. In this regime, BDWFs are less efficient since the uv-bins are elongated. Fig. 13 shows that this translates into less source supression outside the FoI, but does not impact the ability to retain FoI.

---

[2] `http://www.evlbi.org/cgi-bin/EVNcalc`

6   CONCLUSIONS AND FUTURE WORK

The goal of this work was to demonstrate the application of baseline-dependent window functions to radio interferometry. We have demonstrated that BDWFs offer a number of interesting advantages over conventional averaging. The first of these is data compression – i.e. visibilities can be sampled at a lower rate, while retaining a large FoI. Compression by a factor of 16 with relatively little loss of sensitivity has been demonstrated. The huge data rates from upcoming instruments such as ASKAP, MeerKAT and the future SKA1 mean that raw visibilities may need to be discarded after calibration (unlike older instruments, where raw visibilities have typically been archived). This represents something of a risk to the science, as it precludes future improvements in calibration techniques from being later applied to the data. With BDWFs, at least a highly-compressed version of the visibilities may be retained.

The second potential benefit of BDWFs is the increased suppression of unwanted signal from out-of-FoI sources. This reduces both the overall level of far sidelobe confusion noise, and lessens the impact of A-team sources in sidelobes.

Thirdly, BDWFs can have an interesting impact in the VLBI case, as they allow the full primary beam FoI to be imaged using a single VLBI dataset. This opens the door to wide-field VLBI, which has herefore been impractical.

BDWFs have a number of potential downsides. The first one is a potential loss in sensitivity. Our simulations show that this can be kept within reasonable limits, especially if overlapping BDWFs are employed, and can be traded off with compression rate. Note that from DSP theory, we know
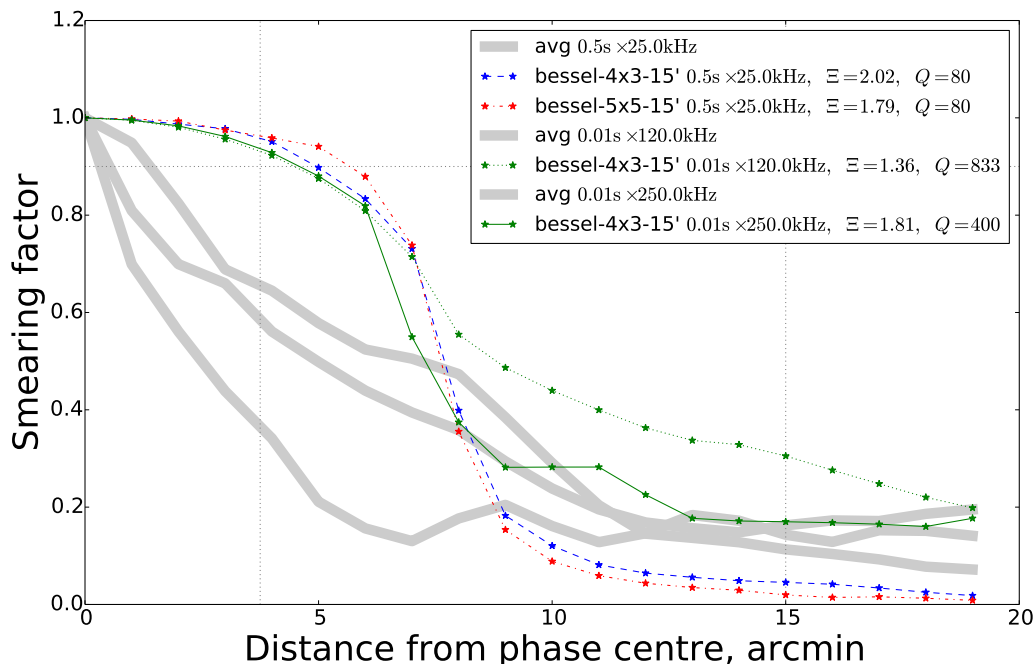
Figure 13. VLBI simulation (10161km maximum baseline) at 1.6 GHz. Smearing as a function of distance from phase centre, for conventional averaging at 0.5s×25kHz, 10ms×120kHz and 10ms×250kHz averaging, and overlapping Bessel BDWFs. The horizontal line corresponds to 10% smearing losses. The ratio Q shows the increase in data volume over conventional 2s×0.5MHz averaging.

that a properly matched filter can actually increase the SNR: the equivalent result with BDWFs is that off-axis sources are attenuated less, so the effective SNR off-axis can increase despite the loss in absolute sensitivity.

The second downside of BDWFs is an increase in computational complexity. Whether implemented in a correlator or in post-processing, BDWFs (and especially overlapping BDWFs) require substantially more operations than simple averaging. There may be other limits to the practical applicability of BDWFs. They are far less efficient if high spectral resolution is required, so their use may be limited to continuum observations. Furthermore, averaging over longer intervals requires accurate phase calibration, so high compression rates may only be achievable post-calibration.

An interesting avenue of future research is combining BDWFs with baseline-dependent averaging. As we saw above, the ability of BDWFs to shape a FoI is somewhat limited by the fact that shorter baselines sweep out smaller bins in uv-space, with window functions over them becoming boxcar-like. If baseline-dependent averaging is employed, shorter baselines are averaged over larger uv-bins, thus increasing the effect of BDWFs.

Finally, we should note that the use of BDWFs results in a different position-dependent PSF than regular averaging (or to put it another way, the smearing response of BDWFs results in a different smeared PSF shape). Future work will focus on methods of deriving this PSF shape, with a view to incorporating this into current imaging algorithms.

REFERENCES

Bregman J. D., 2012, PhD thesis, Ph. D. Thesis, University of Groningen, Groningen, The Netherlands, pp81-82

Bridle A., Schwab F., 1999, in Synthesis Imaging in Radio Astronomy II Vol. 180, Bandwidth and time-average smearing. p. 371

Bridle A. H., Schwab F. R., 1989, in Synthesis Imaging in Radio Astronomy Vol. 6, Wide field imaging i: Bandwidth and time-average smearing. p. 247

Delsarte P., Janssen A., Vries L., 1985, SIAM Journal on Applied Mathematics, 45, 641

Keimpema A., Kettenis M., Pogrebenko S., Campbell R., Cimó G., Duev D., Eldering B., Kruithof N., van Langevelde H., Marchal D., et al., 2015, Experimental Astronomy, pp 1–21

Noordam J. E., Smirnov O. M., 2010, A&A, 524, A61

Nuttall A. H., Carter G. C., 1982, Proceedings of the IEEE, 70, 1115

Offringa A. R., de Bruyn A. G., Zaroubi S., 2012, MNRAS, 422, 563

Perley R., 2013, High Dynamic Range Imaging, presentation at "The Radio Universe @ Ger's (wave)-length" con-
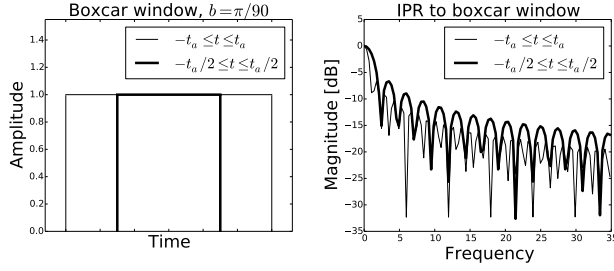
Figure A1. Boxcar and its IPR.
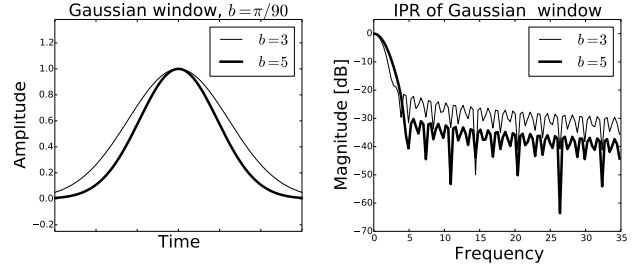
Figure A2. Gaussian and its IPR.
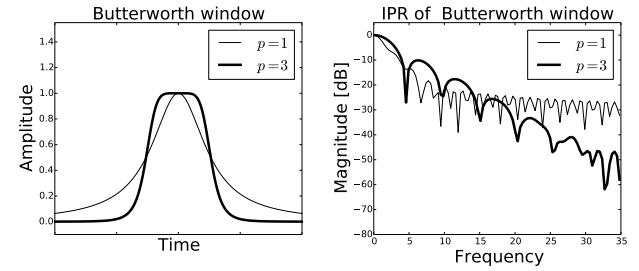
Figure A3. Butterworth and its IPR.

ference (Groningen, November 2013), http://www.astron.nl/gerfeest/presentations/perley.pdf

Podder P., Khan T. Z., Khan M. H., Rahman M. M., 2014, International Journal of Computer Applications, 96

Smirnov O. M., 2011, Astronomy & Astrophysics, 527, A106

Smirnov O. M., Frank B., Theron I. P., Heywood I., 2012, in Int. Conf. on Electromagnetics in Advanced Applications (ICEAA 2012). 2-7 September. Cape Town, South Africa Understanding the impact of beamshapes on radio interferometer imaging performance

Thompson A. R., 1999, in Synthesis Imaging in Radio Astronomy II Vol. 180, Fundamentals of radio interferometry. p. 11

Thompson A. R., Moran J. M., Swenson, Jr. G. W., 2001, Interferometry and Synthesis in Radio Astronomy, 2 edn. Wiley, New York

Van Haarlem M., Wise M., Gunst A., Heald G., McKean J., Hessels J., De Bruyn A., Nijboer R., Swinbank J., Fallows R., et al., 2013, Astronomy & astrophysics, 556, A2

Walter G., Soleski T., 2006, Sampling theory in Signal and Image Processing, 5, 21

Watson G. N., 1995, A treatise on the theory of Bessel functions. Cambridge university press

Wrobel J., Walker R., 1999, in Synthesis Imaging in Radio Astronomy II Vol. 180, Sensitivity. p. 171

APPENDIX A: OVERVIEW OF WINDOW FUNCTIONS

A1 Boxcar window

The boxcar window for a cut-off time interval of $[-t_a, t_a]$ is defined as:

$$\Pi(t/t_a) = \begin{cases} 1 & -t_a \leqslant t \leqslant t_a \\ 0 & \text{otherwise} \end{cases} \qquad (A1)$$

Fig. A1 shows a plot of $\Pi(t/t_a)$ and its IPR. The thick grey and thin curves correspond to cut-off time intervals of $[-t_a, t_a]$ and $[-t_a/2, t_a/2]$ respectively. Note that when the cut-off time interval is larger, the MLW is narrower, and the sidelobes are lower.

The other window functions given below are all multiplied with a boxcar to ensure a cut-off interval of $[-t_a, t_a]$.

A2 Gaussian window

A Gaussian window function centred at zero with a standard deviation of σ_1 is given by:

$$G(t) = \Pi(t/t_a)e^{-bt^2}, \qquad (A2)$$

where $b = (2\sigma_1^2)^{-1}$. The Fourier transform of the Gaussian term is given by $\mathcal{F}\{G\} = \sqrt{\frac{b}{\pi}}e^{-cl^2}$, where $c = \pi^2/b$, i.e. is also a Gaussian with standard deviation of $\sigma_2 = (2\pi\sigma_1)^{-1}$.

Fig. A2 shows a plot of $G(t)$ and its IPR. The window function is truncated at $[-t_a, t_a]$, with $b = 3$ for the thin curve and $b = 5$ for the thick grey curve. Its response is characterized by extremely low sidelobes, but a narrow main lobe.

A3 Butterworth window

A Butterworth window function is flat in the time pass band, and rolls off towards zero in the time stop band and it is characterized by two independent parameters, the cut-off time time $[-t_a, t_a]$ and the order p. The two parameters control the FoI and sidelobes attenuation. The Butterworth window function is given by:

$$\text{BW}(t) = \Pi(t/t_a)\Big(1 + (t/t_a)^{2p}\Big)^{-1}. \qquad (A3)$$

Fig. A3 shows Butterworth window functions for the same cut-off interval $[-t_a, t_a]$, with orders of $p = 1, 3$. Note that increasing the order p conserves the MLW, and dramatically lowers distant sidelobes, at the cost of pushing up the near-in sidelobes

A4 Prolate spheroidal window

This window function is given by a prolate spheroidal wave function of sequence zero ($n = 0$) characterized by two independent parameters, the cut-off time $[-t_a, t_a]$ and the order
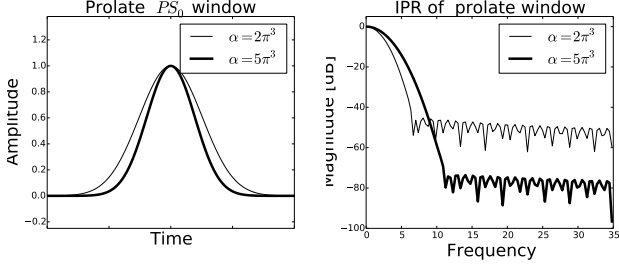
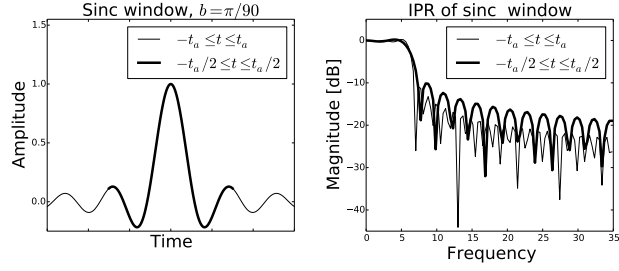**Figure A4.** Prolate window (of oder zeros) and its IPR.

Figure A6. J_0 and its IRP.

Figure A5. Sinc and its IPR.

Figure A7. Sinc-Hamming and it IPR.

α (Delsarte et al. 1985; Walter & Soleski 2006). The two parameters control the FoI and sidelobes attenuation. The prolate spheroidal wave function PS_0 is the eigenfunction and solution of the integral:

$$\int_{-t_a}^{t_a} PS_0(\xi) \frac{sin(\frac{\alpha}{\pi}(t-\xi))}{\frac{\alpha}{\pi}(t-\xi)} d\xi = \lambda_{n=0,\alpha,t_a} PS_0(t), \qquad \text{(A4)}$$

where $\lambda_{n=0,\alpha,t_a}$ is the coresponding eigenvalue. Fig. A4 shows prolate spheroidal window functions for the same cut-off interval $[-t_a, t_a]$, with orders of $\alpha = 2\pi^3, 5\pi^3$. Note that increasing the order α increases the MLW, and dramatically lowers sidelobes.

A5 Sinc window

The sinc window function is defined as

$$\text{Sinc}(t) = \Pi(t/t_a) \frac{\sin(\pi b t)}{\pi b t}. \qquad \text{(A5)}$$

Fig. A5 shows $\text{Sinc}(t)$ for a fixed value of b, and cut-off intervals given by $[-t_a, t_a]$ and $[-t_a/2, t_a/2]$. Note that the IPR of a sinc window function is almost perfectly flat in the main lobe (more so for larger intervals). The sidelobe response is relatively poor, but better for larger intervals.

A6 Bessel J_0 window

This window function is given by a Bessel function of the first kind of order zero (Watson 1995). Using a power series expansion, we have:

$$J_0(t) = \Pi(t/t_a) \sum_{k=0}^{\infty} \frac{(-1)^k (t/2)^{2k}}{(k!)^2}. \qquad \text{(A6)}$$

Fig. A6 shows $J_0(t)$ and its IPR, with $J_0(t)$ truncated at time intervals $[-t_a, t_a]$ and $[-t_a/2, t_a/2]$. The performance
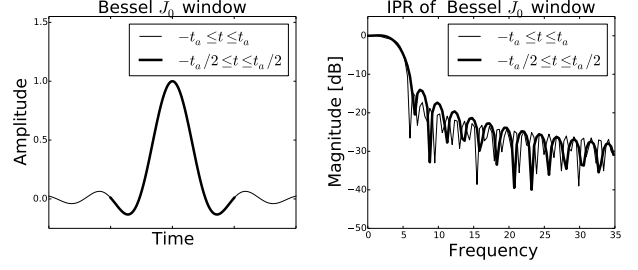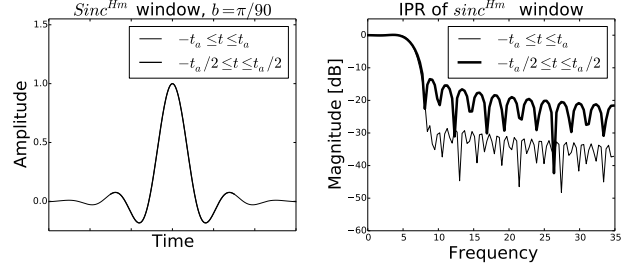
of J_0 is somewhat worse than the sinc within the main lobe, and somewhat better in the sidelobes.

A7 Sinc-Hamming and J_0-Hamming windows

The Hamming, Han or Blackman filter is sometime multiplied by a $J_0(t)$ or $\text{Sinc}(t)$ to increase the pass band (FoI) and increase the stop band (outside the FoI) attenuation. The process can be resume as follow:

$$Y^{\text{X}} = Y(t)X(t) \qquad \text{(A7)}$$

where $X(t)$ is either the Hamming (Hm), Han (Hn) or Blackman (B) window functions well known in SP litterature (Nuttall & Carter 1982; Podder et al. 2014) and Y is a $J_0(t)$ or $\text{Sinc}(t)$ window function. Fig. A7 and A8 show the Sinc^{Hm} and the J_0^{Hm} window functions and their IPRs. Compared to the $\text{Sinc}(t)$ and $J_0(t)$, they show lower PSL and higher SLR.

A8 Relative Performance of Window Functions

Window functions – or rather their corresponding image-plane response (IPR) – can be characterized in terms of
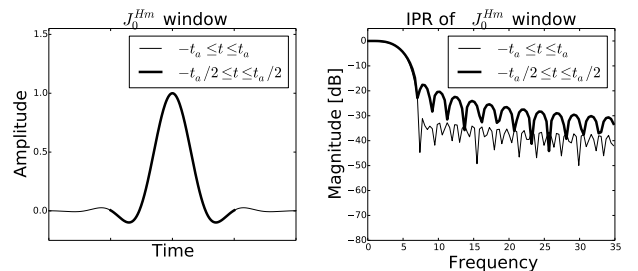
Figure A8. Bessel-Hamming and it IPR.

window functions		~MLW (deg and at -3dB)	PSL (dB)	SLR (dB/oct)
$\Pi(t/t_a)$	$t \in \lvert t_a \rvert$	1.406	−6.663	−12.089
	$t \in \lvert t_a/2 \rvert$	2.812	−6.671	−11.065
$\text{Sinc}(t)$	$t \in \lvert t_a \rvert$	12.304	−10.889	−12.661
	$t \in \lvert t_a/2 \rvert$	12.304	−13.241	−11.447
$J_0(t)$	$t \in \lvert t_a \rvert$	9.140	−14.553	−12.011
	$t \in \lvert t_a/2 \rvert$	9.140	−13.614	−11.794
G(t)	b=3	2.109	−21.535	−9.589
	b=5	2.812	−30.211	−9.091
BW(t)	p=1	2.109	−13.718	−12.581
	p=3	4.218	−10.145	−27.330
$PS_0(t)$	$\alpha = 2\pi^3$	3.515	−45.302	−7.424
	$\alpha = 5\pi^3$	4.218	−73.597	−6.375
$J_0^{\text{Hm}}(t)$	$t \in \lvert t_a \rvert$	9.140	−35.724	−11.948
	$t \in \lvert t_a/2 \rvert$	9.140	−22.670	−19.527
$Sinc^{\text{Hm}}(t)$	$t \in \lvert t_a \rvert$	12.656	−27.581	−13.817
	$t \in \lvert t_a/2 \rvert$	12.656	−13.469	−14.324

Table A1. Comparative performance of different window functions. MLW: main lobe width, PSL: peak sidelobe level, SLR: sidelobes roll-off.

various metrics. Some common ones are the peak sidelobe level (PSL), the main lobe width (MLW) and the sidelobes roll-off (SLR) rate. In terms of the "ideal" IPR (Fig. 2, left), these correspond to the following desirable traits:

• Maximally conserve the signal within the FoI ("passband" in the figure), and make the transition region as sharp as possible. Both of these correspond to larger MLW.
• Attenuate sources outside the FoI ("stopband"): this corresponds to a lower PSL and higher SLR.

Table A1 summarizes the performance of the different window functions. This table shows that the sinc, the Bessel and all their derivative with Hamming, Han and Blackman window functions have large main lobe, low peak sidelobe level and high sidelobes roll-off and therefore provide the more optimal tapering response.

This paper has been typeset from a TEX/ LATEX file prepared by the author.